Metadata of the chapter that will be visualized in SpringerLink

Book Title	Clean Energy Conversion	
Series Title		
Chapter Title	Atomistic Simulations	
Copyright Year	2025	
Copyright HolderName	The Author(s)	
Corresponding Author	Family Name	**Schnieder**
	Particle	
	Given Name	**Bastian**
	Prefix	
	Suffix	
	Role	
	Division	Chair for Theoretical Chemistry
	Organization	Ruhr-Universität Bochum
	Address	Bochum, NRW, Germany
	Email	bastian.schnieder@ruhr-uni-bochum.de
Author	Family Name	**Jahromi**
	Particle	
	Given Name	**Babak Farhadi**
	Prefix	
	Suffix	
	Role	
	Division	Chair for Inorganic Chemistry II
	Organization	Ruhr-Universität Bochum
	Address	Bochum, NRW, Germany
	Email	babak.farhadi-Jahromi@rub.de
Author	Family Name	**Schmitz**
	Particle	
	Given Name	**Gunnar**
	Prefix	
	Suffix	
	Role	
	Division	Chair for Inorganic Chemistry II
	Organization	Ruhr-Universität Bochum
	Address	Bochum, NRW, Germany
	Email	gunnar.schmitz@rub.de
Author	Family Name	**Hättig**
	Particle	
	Given Name	**Christof**
	Prefix	
	Suffix	

	Role	
	Division	Chair for Theoretical Chemistry
	Organization	Ruhr-Universität Bochum
	Address	Bochum, NRW, Germany
	Email	christof.haettig@rub.de
Author	Family Name	**Schmid**
	Particle	
	Given Name	**Rochus**
	Prefix	
	Suffix	
	Role	
	Division	Chair for Inorganic Chemistry II
	Organization	Ruhr-Universität Bochum
	Address	Bochum, NRW, Germany
	Email	rochus.schmid@rub.de

Abstract

Efficient solid fuel combustion models use semi-global mechanisms with effective parameters, traditionally derived from a small set of reference fuels and conditions. This limits their transferability. Atomistic simulations can compute thermodynamic properties such as reaction enthalpies and adsorption energies. This enables the determination of rate coefficients for elementary reaction steps and diffusion constants across a broad range of temperatures and pressures, including those inaccessible to experiments. Unlike empirical data tied to specific fuels, kinetic parameters from simulations depend on molecular composition and structure. This allows for seamless kinetic models applicable to different solid fuels. Computational results on diffusion and adsorption also complement experiments, aiding the development of improved sorption models. To achieve this, various computational chemistry tools are employed. Char models are built using reactive and non-reactive molecular dynamics. Small molecule diffusivity is isolated via non-reactive simulations, while reactive dynamics combined with molecular graph analysis are used to identify possible reaction pathways. Accurate electronic structure methods are used to compute rate coefficients.

Author Proof

Check for updates

Atomistic Simulations

7

Bastian Schnieder, Babak Farhadi Jahromi, Gunnar Schmitz, Christof Hättig and Rochus Schmid

UNCORRECTED PROOF

Contents

7.1 Introduction 2
7.2 Non-Reactive Processes 5
7.2.1 Construction of Atomistic Char Models 6
7.2.2 Simulation of Diffusion in Char 9
7.3 Reactive Processes 11
7.3.1 Multi-Method Approach for Reaction Networks and Rate Coefficients 12
7.3.2 Reaction Discovery with Reactive MD 16
7.3.3 Initial Reactions and Influence of Functional Groups 19
7.3.4 Break-Down of the Carbon Framework 23
7.4 Conclusion 25
References 26

Abstract

Efficient solid fuel combustion models use semi-global mechanisms with effective parameters, traditionally derived from a small set of reference fuels and condi-

B. Schnieder (✉) · C. Hättig
Chair for Theoretical Chemistry, Ruhr-Universität Bochum, Bochum, NRW, Germany
e-mail: bastian.schnieder@ruhr-uni-bochum.de

C. Hättig
e-mail: christof.haettig@rub.de

B. F. Jahromi · G. Schmitz · R. Schmid
Chair for Inorganic Chemistry II, Ruhr-Universität Bochum, Bochum, NRW, Germany
e-mail: babak.farhadi-Jahromi@rub.de

G. Schmitz
e-mail: gunnar.schmitz@rub.de

R. Schmid
e-mail: rochus.schmid@rub.de

© The Author(s) 2025

R. Kneer et al. (eds.), *Clean Energy Conversion*,
https://doi.org/10.1007/978-3-031-98956-8_7

609647_1_En_7_Chapter-online ☑ TYPESET ☐ DISK ☐ LE ☑ CP Disp.:20/9/2025 Pages: xxx Layout: German_T1

Author Proof

tions. This limits their transferability. Atomistic simulations can compute thermodynamic properties such as reaction enthalpies and adsorption energies. This enables the determination of rate coefficients for elementary reaction steps and diffusion constants across a broad range of temperatures and pressures, including those inaccessible to experiments. Unlike empirical data tied to specific fuels, kinetic parameters from simulations depend on molecular composition and structure. This allows for seamless kinetic models applicable to different solid fuels. Computational results on diffusion and adsorption also complement experiments, aiding the development of improved sorption models. To achieve this, various computational chemistry tools are employed. Char models are built using reactive and non-reactive molecular dynamics. Small molecule diffusivity is isolated via non-reactive simulations, while reactive dynamics combined with molecular graph analysis are used to identify possible reaction pathways. Accurate electronic structure methods are used to compute rate coefficients.

7.1 Introduction

Due to its heterogeneous structure, the combustion of (bio)char is an extremely complex process in which various volatile and non-volatile intermediates occur. Heterogeneous and homogeneous reactions are important and, at the elevated temperatures of the combustion, mass transport through the porous char matrix with pores on different length scales plays a central role. Experimentally, reaction parameters of individual reactions are difficult to access. Widely-used simplified reaction models are based on the formulation of net reactions taking into account boundary layer and pore diffusion, and simplified heterogeneous reactions [1,2]. Such models are ultimately required for multi-scale simulations of the whole combustion process. A comprehensive overview of models can be found in a review by Hasse [1]. It is important in this context that the network of homogeneous gas-phase reactions for the combustion of small volatile molecules is known to some extent and rate parameters are often already available [3]. Also, those reactions are mostly fast and can be regarded as approximately being in equilibrium [2].

In contrast, much less data is available at the atomistic level on the slower, heterogeneous reactions for the combustion of (bio)char matrices. It is commonly modelled with a small set of lumped net reactions with Arrhenius-type expressions for temperature dependence. The parameters of such models are usually fitted to experimental data or empirically adjusted to reproduce the product spectrum and overall net reactions rates. However, such models subsume a large number of elementary reactions for chemically different intermediates. Heteroatoms contained in char, such as nitrogen, sulphur, potassium, etc. are usually not accounted for in such models because of missing experimental data.

Similarly, as shown by Hurt and Calo [4], an experimental determination of adsorption and desorption rates is, especially at high temperatures, often not possible due to transport limitations. This makes it very difficult to disentangle experimentally the contributions from different processes to determine the actual reaction rates

UNCORRECTED PROOF

Author Proof

for individual elementary steps. In addition, effects such as change in pore structure, thermal deactivation of the char by annealing, or reduction of the apparent reaction rate with increasing ash content during combustion can only be taken into account by very simple approaches with empirically adjusted parameters.

Theoretical methods with atomistic resolution can provide results for elementary steps that are not easily accessible by experiments but needed to separate contributions from different reaction channels. So far, there are only a few studies that have investigated individual elementary reactions of char combustion in this way [5]. First with the advances in theoretical models and the rapid development of computer architectures in recent years such complex reaction systems became accessible for a theoretical modelling at the atomistic and elementary reaction level.

Pioneering in this field has been the joint work of the developers of the reactive force field ReaxFF [6] around van Duin and the group of Mathews, who used molecular dynamics (MD) simulations to model the combustion of an atomistic char model [7]. By combining different sizes of condensed aromatic compounds with stochastically distributed functional groups, they constructed an atomistic model with almost 10,000 atoms for which they subsequently simulated the combustion in a pure oxygen atmosphere. This study demonstrated the possibilities of theoretical calculations and the mechanistic insights that could be obtained from simulations at that time. However, the accuracy of the reactive force field was quite limited. To make the MD simulation feasible, very high temperatures of 3000–4000 K were used to accelerate the computations. The conclusions that can be drawn from such a study based on a single theoretical method and brute force MD, are therefore limited. Nevertheless, this work represented an important feasibility study for the use of reactive force fields.

As a result of the development mentioned above, the treatment of larger systems is now possible at the same accuracy that before was only achievable for small gas-phase species. The determination of reaction energies is now possible with chemical accuracy for systems with 30 or more atoms, provided the molecular structure is well-defined. This is commonly used for homogeneous gas phase reactions of small molecules. However, due to the complex amorphous and hierarchical structure of (bio)char and the coupling of heterogeneous combustion and gasification reactions to mass transport through pores on different length scales, a direct brute force simulation at the atomistic level is still out of reach. There is no question that theoretical modelling of char combustion aiming at predictive accuracy required also at the atomistic level a multi-scale approach. Only by combining different specialised methods with varying degrees of accuracy for different intra- and intermolecular interactions and, thus, varying computational demands with length- and time-scale bridging approaches, the complex processes during char burn out can be captured.

Besides such a multi-scale and multimethod approach, a heuristic methodology to generate realistic structure models with atomic resolution is needed as starting point to simulate transport processes of small molecules and as a stage to investigate reactive processes during combustion. Generating such models presents several significant challenges due to the complex heterogeneous nature of the material. Char exhibits regions of high graphitisation, but also contains numerous defects that

UNCORRECTED PROOF

Author Proof

disrupt these ordered domains. Additionally, char is interspersed with various functional groups containing elements such as oxygen, nitrogen, sulphur, etc., adding to its chemical complexity. The pyrolysis process creates voids of varying sizes within the char, as the volatile gases are released, further contributing to the irregular and multifaceted nature of its structure. Up to now, char models have mainly been generated ad hoc or by semi-automatic assembling of small graphitic units (flakes) with a moderate amount of non-planar defects [8]. In the present work, an entirely new strategy has been explored to arrive at realistic char models, which is rooted on exploiting ReaxFF to anneal and relax initial structures towards chemically meaningful molecular systems. The approach allows to incorporate experimental information like density, flake size and tortuosity, or concentration of functional groups as boundary conditions into the generation process.

A computational workflow has been developed to produce different stacks of defect-rich graphitic carbon with a predefined size and corrugation. Different functional groups can be distributed in an automated fashion. From these graphitic stacks, or from fragments of these, larger structure models are generated using periodic boundary conditions. Here, a geometric analysis of the pore size distribution allows again comparison with experimental data.

With an increasing size of these structure models in terms of the number of atoms, even the use of rather efficient methods like the reactive force field ReaxFF becomes computationally intractable. In addition, they are not specifically calibrated to reproduce non-bonded interactions. Thus, at these larger length and timescales, where a realistic and chemically meaningful atomistic structure has already been realised, non-reactive generic force fields are employed to investigate transport properties of small gas molecules like oxygen, nitrogen, carbon dioxide, or water. In addition, as a benchmark, also idealised slit pores of differently functionalised graphitic surfaces have been used to study adsorption and diffusion of gaseous molecules.

Due to its high computational performance, ReaxFF is also used extensively in the current study to discover possible reaction pathways. Because of the approximations that are made to achieve the computational performance that is needed for MD simulations, the accuracy of ReaxFF is not sufficient to obtain quantitative results for reaction energies or realistic reaction rates. The latter require accurate electronic structure methods based on a quantum mechanics that are computationally demanding. To bridge the gap between accurate electronic structure methods and the reaction discovery that is done with MD simulations combined with a qualitative method for the potential energy surface, a tool for the analysis of MD trajectories is implemented that automatically detects reaction events and stores them in a database (see below). They serve then as starting points for step-wise refinements of reaction pathways, molecular structures, energies, and entropies that employ electronic structure methods of increasing accuracy and computational demands. It starts with density functional theory (DFT) at the meta generalised gradient approximation (meta-GGA) level followed by a further refinement with a hybrid functional, and explicitly correlated coupled-cluster calculations for the final energies. This combination of methods allows to compute reaction and activation energies with an accuracy of a few kilojoules per mole. The vibrational energy levels are used in combination with a quasi

UNCORRECTED PROOF

Author Proof

rigid rotor harmonic oscillator (qRRHO) approximation [9,10] to compute the partition functions needed for reaction rates and entropy contributions to free energies.

Although, as a force field approach, ReaxFF stands out by its high performance for reactive MD simulations it has some shortcomings that limits its applicability for char combustion modelling. One of them is that parameterisations suitable for combustion conditions are not yet available for some atom types that are relevant for char combustion like phosphorus, Ca, K, and Na. Also, as a force field approach, ReaxFF is not aware of the electronic structure and thus of information like the number of electrons or the electronic spin. Therefore, extended tight binding methods from the GFN-xTB family [11] are explored as semi-empirical electronic structure methods as alternative approaches for reactive MD simulations for reaction discovery.

As mentioned above, (bio)char consists of interlinked polyaromatic hydrocarbons (PAHs), functionalised in particular with oxygen, but also with nitrogen and sulphur containing functional groups. The functional groups occur mostly at the edge of the aromatic regions and are the most important points of attack during oxidation. But also hydrogen atoms at the edge of aromatic ring systems can be abstracted by highly reactive radicals like H and O atoms that are present at the elevated temperatures in the combustion atmosphere. The organic radicals that are generated by these initial steps can react with molecular oxygen—which is otherwise not very reactive—and form organic peroxo radicals that play a central role in radical chain branching.

The atomistic simulations are separated into reactive and non-reactive processes in the ensuing sections.

7.2 Non-Reactive Processes

For the char-burnout mechanism, the heterogeneous combustion and gasification reactions are crucial. However, due to the entanglement of the chemical reactions with transport processes, also this aspect needs to be considered in atomistic simulations. In particular the transport of small molecules like oxygen, carbon dioxide or water as well as the transport of heat (or the heat capacity) can be determined by molecular dynamics simulations. From an experimental point of view, transport properties like diffusion constants can be determined, however, not for the conditions during char burnout. It is an advantage here that theoretical simulations allow on one side to extrapolate such properties to, e.g. high temperature conditions, but at the same time to constrain the systems not to undergo any chemical reactions, which allows in the end to disentangle transport and reactive contribution to effective rates. However, as pointed out above, a required prerequisite for such simulations are appropriate atomistic structure models for char. From a methodological point of view, also more efficient non-reactive force field methods need to be implemented, capable to describe the complex chemical environments found in the amorphous char.

UNCORRECTED PROOF

Author Proof

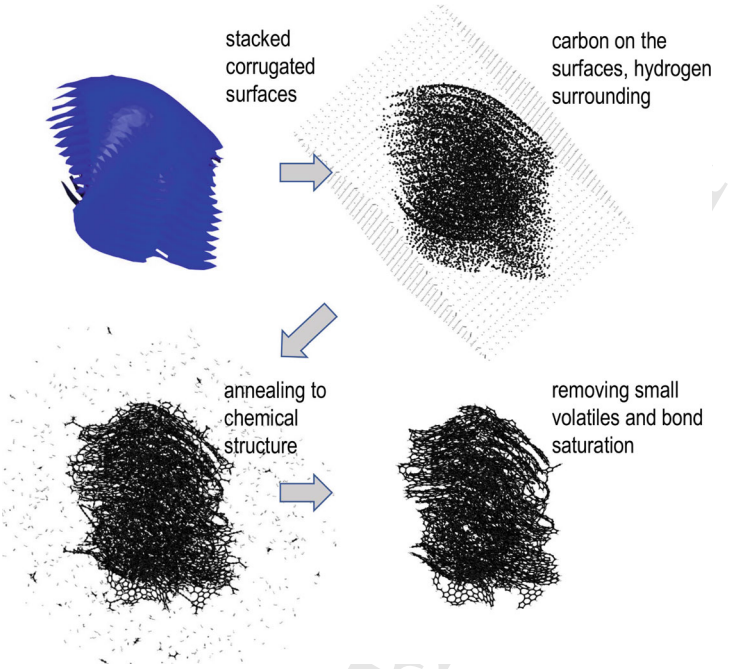


Fig. 7.1 Schematic visualisation of the top-down method for the construction of stacked char models using curved meshes as blueprints

7.2.1 Construction of Atomistic Char Models

The basic workflow of the newly developed char construction methodology [12] is visualised in Fig. 7.1. It begins with a curved mesh as primary input, for which parameters like size and corrugation should in practice be derived from experimental HRTEM data. Stacked meshes are then formed by extrapolating mesh points from the initial mesh via its normal vectors with certain geometric constraints, most importantly a 3.5 Å distance of the new points to the initial mesh to reproduce the experimentally observed distance of stacked graphene sheets. This procedure is continued until the desired stack size is obtained.

Then, carbon atoms are randomly placed on each of these templating surfaces in the stack with the number of carbon atoms slightly below the atomic surface density of graphene. An adequately sized simulation box is then spanned around the stacked carbon atoms and the empty space is populated with hydrogen atoms at least 3 Å apart from each carbon atom in the stack.

The transformation of the resulting system into a chemically reasonable char model is initialised by a restrained energy minimisation of the system using ReaxFF, where the atoms are allowed to structurally relax under the restraint of harmonic spring potentials that force the carbon atoms to their respective mesh planes. Next, the system is dynamically restructured in a MD simulation employing ReaxFF that consists of a 25 ns long heating stage towards 2500 K followed by a 25 ns long

UNCORRECTED

Author Proof

Table 7.1 Parameters of the three char single planes formed on meshes generated from Gaussian hill functions

Name	GH15	GH20	GH25
Gaussian height/Å	15	20	25
Empirical formula	$C_{2038}H_{313}$	$C_{2102}H_{376}$	$C_{2104}H_{360}$

annealing stage at 2500 K and a final 2.5 ns long quenching stage towards 100 K during which the system freezes into a chemically reasonable structure.

The frozen structure is relaxed in an energy minimisation and refined with an algorithm which identifies and modifies energetically unfavorable structural features. First, regardless of the actual element, atoms bonded to only a single other atom are replaced by hydrogen, the remaining atoms are considered carbon. Next, carbon atom pairs with interatomic distances below 1 Å are fused into a single carbon atom with an averaged position. Next, 3-membered carbon rings are opened by removing single members and saturating with hydrogen atoms, where appropriate. The remaining undercoordinated carbon atoms are also saturated with hydrogen atoms if the surrounding steric bulk allows it, else they are kept as radicals. Molecules with less than 20 atoms are considered to be volatile species and are removed. Finally, the system is again allowed to relaxed via energy minimisation using ReaxFF to yield a chemically stable char model. This refinement process can be reiterated multiple times if required.

The presented workflow is robust to arbitrary mesh curvatures, which is demonstrated by the application on input meshes generated from two-dimensional Gaussian functions with heights given in Table 7.1. Truncating the process after the formation of the initial layer yields the char monosheets displayed in Fig. 7.2. These achieve the desired curvatures in a chemically plausible fashion by formation of several types of defects with respect to pristine graphene sheets. On the one hand, certain local curvatures are achieved by the incorporation of 4- to 8-membered carbon rings, on the other hand the formation of holes in the monosheet increases local flexibility around the holes allowing for certain curvatures.

Based on the foundational char models obtained by this workflow, more realistic char models can be derived by taking experimental data into account, specifically the fringe lengths of real char flakes computed from HRTEM images and the amount of functional groups from TPD measurements. The distribution of such measured fringe lengths serve as the experimental anchor data for the developed second generation of char models. These are generated by first cutting out stacks of three to five carbon layers from the initial model with fringe lengths in the range of the experimentally measured values. These cutouts then undergo a series of refinement steps before they are finally recombined to a realistic char model. In the first algorithmic refinement step, oxygen-carrying functional groups are hierarchically introduced by replacing carbon and hydrogen atoms at suitable sites identified by the algorithm until a functional group distribution close to experiment is reached. A functionalised char stack obtained form this procedure is displayed in Fig. 7.3.

UNCORRECTED PROOF

Author Proof

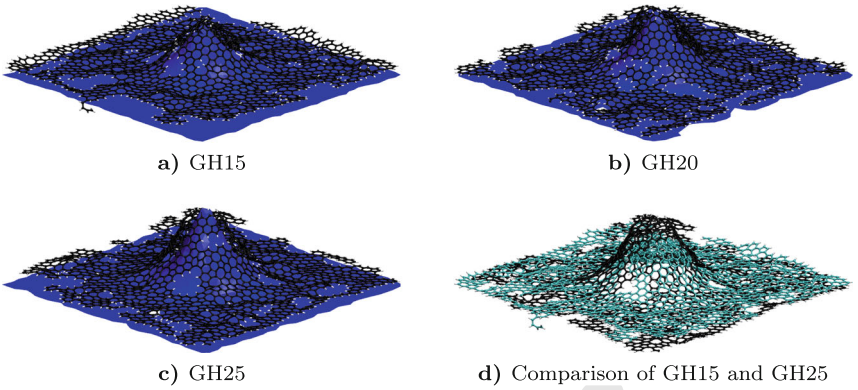


Fig. 7.2 Char single planes with meshes generated from Gaussian hills of three different heights (reprinted from Angenent et al. [12], licensed under CC BY-SA 4.0)

Following the oxygen functionalisation, the geometries of the char stacks are optimised using GFN2-xTB [11] to remove structural artifacts introduced by all preceding construction steps, for example by quenching radicalic sites through inter-layer bond formation or by resolving overcoordination via bond breaking, which may result in elimination of small molecules that are subsequently purged from the stack. A realistic char model is then obtained by positioning a large number of optimised stacks of varying size and shape in a periodic simulation box as displayed in Fig. 7.3. Here, the PACKMOL [13] package was used for the positioning.

Due to the large system size that is needed for realistic char models constructed in this fashion, any further processing and, more importantly, MD simulation of these at time scales that are sufficiently long to cover relevant dynamical properties requires a potential energy model that is computationally more efficient than ReaxFF. For sampling phenomena that do not involve the breaking of chemical bonds, such as adsorption and diffusion of small molecules in char, the reactivity of ReaxFF can be traded for efficiency by employing a non-reactive force field. Further more, ReaxFF is not calibrated for the non-bonded interactions important for diffusion and adsorption

Furthermore

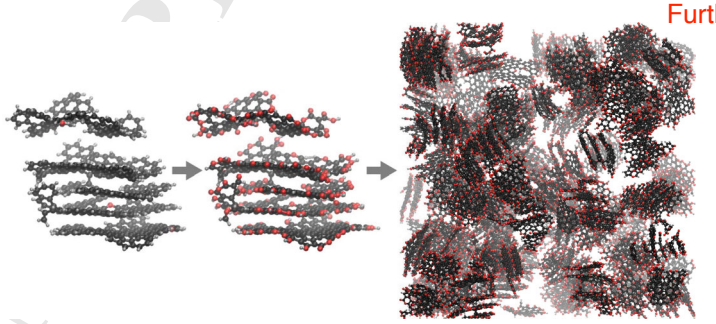


Fig. 7.3 Examples for oxygen functionalisation of a stack of small char flakes and for a porous char model consisting of 92 unique functionalised stacks with in total system size of 27,907 atoms and a box length of 109.1 Å

609647_1_En_7_Chapter-online ☑ TYPESET ☐ DISK ☐ LE ☑ CP Disp.:20/9/2025 Pages: xxx Layout: German_T1

Author Proof

in the char matrix. To this end, the generic UFF [14] was employed, which uses a rule-based system to generate force field parameters for the entire periodic table from a set of purely atomic parameters. However, due to the chemical complexity of char it could not be used unmodified because of particular chemical environments present in char models that UFF was not designed for, such as certain three and four-membered rings, allenes, and ketenes, some of which are to be expected in functionalised char and some being artificially favoured by ReaxFF which was used for the initial char construction steps. With respect to the latter, some rather reactive sites contained in the constructed char models can be traced back to insufficient saturation with hydrogen in the initial construction steps, which could not be fully quenched by the reoptimisation with GFN2-xTB. To remedy this, certain modifications to UFF had to be made, such as extending the generic rules for the setup of the UFF potential terms when such chemical environments are identified, as well as entirely eliminating certain potential energy contributions that turn numerically instable in edge cases that are frequently encountered in the generated char models. The atom types that dictate the setup rules for UFF are reliably identified using the *Open Babel* [15] package. For the electrostatic contributions to the potential energy, rather than using a fluctuating charge model based on charge equilibration [16] as in the standard UFF, the modified UFF uses a simple static point charge model, that enters the potential energy via Coulombic interaction terms between these, located at the respective atomic sites. The atomic partial charges are initialised by a topological charge equilibration model (QEq) developed by some of the authors of this chapter, which allows the use of realistic, well-balanced charges independent of the geometry to reduce the numerical effort. Such an electrostatic model is of prime importance to capture, e.g. the non-bonded quadrupole interaction of CO_2 with the char matrix. The parametrisation for the topological QEq model has been generated from a large set of reference data for porous hybrid materials with a wide variety of chemical environments.

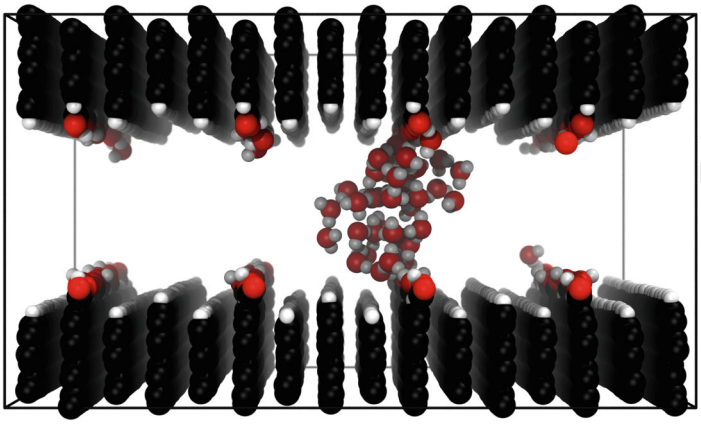
The above workflow allows now to construct realistic char models with periodic boundary conditions, using corrugated, yet stacked graphitic planes with the ability to systematically vary stack sizes, functional groups and defect concentrations. Densities and pore size distributions can be adjusted either by choosing differently sized stacks or by further compressing the models alongside with an annealing sequence. The implementation of an extended UFF setup allows efficient non-reactive MD simulations to target (mixture) adsorption, and diffusion also at experimentally inaccessible conditions as, e.g. the higher temperatures of char combustion.

7.2.2 Simulation of Diffusion in Char

In Chap. 5, the impact of oxygen functionalisation of char on the adsorption and diffusion of water is investigated experimentally [17], indicating a stronger interaction of water with the functionalised hydrophilic interface as compared to the more hydrophobic native char. To shed light on this behaviour on a molecular level, an idealised scenario has been investigated by non-reactive force field simulations. Since the major part of carbon in char appears as graphitic stacks, it was chosen to use a

UNCORRECTED PROOF

Author Proof



for a water concentration

Fig. 7.4 Idealised graphite slit pore. The COOH-terminated 2-D graphite slab with a pore width of 14 Å is shown for the a water concentration of around 2.0 mol L^{-1} of water, viewed in x direction

highly idealised surface, namely a hydrogen terminated 2-D slab of ideal crystalline graphite. By slicing the crystal structure of graphite in different hkl-planes, either zig-zag or armchair type surfaces are formed. Note, that the entirely hydrophobic graphene-like interface was intentionally omitted, since it can not be functionalised. The dangling bonds resulting from this slicing have been saturated with hydrogen atoms. For the functionalised variant of the 2-D slab, a number of these bonds have instead been saturated with carboxylic acid (COOH) groups (54 groups in the simulation box). This is roughly equivalent to the estimated number of functional groups per surface area determined from the experimental measurements on the high-functionalised model char O-MH800 which is based on the native MH800 [18] char. In this setup, the z direction is the surface normal, whereas x and y are defined to be parallel and perpendicular to the graphene sheets, respectively (see Fig. 7.4).

pore width of 14 ...

Figure 7.4 shows the simulation setup for a pore width of ~~5 and~~ 14 Å and a low water concentration. In addition, a very wide 100 Å slit pore geometry has been co

In addition, a narrow 5 Å, and a very wide 100 Å split pore have been considered.

up

Note, that the actual pore volume needed to determine the concentrations are approximated using the pore width, which is measured between the saturating hydrogen atoms as shown in Fig. 7.4. The generic force field UFF [14] was used for the graphite slabs together with the SPC/Fw flexible water potential [19]. The slit pores have been loaded with water molecules and, using MD simulations in the NVT ensemble, the molecular trajectories of the water molecules were determined. From Einstein's diffusion equation, the water self-diffusion constants D_{H_2O} can be derived via the slope of the mean square displacement MSD

$$MSD(t) = \frac{1}{N} \sum_{i=1}^{N} [\mathbf{r}_i(t) - \mathbf{r}_i(0)]^2 , \tag{7.1}$$

UNCORRECTED

Author Proof

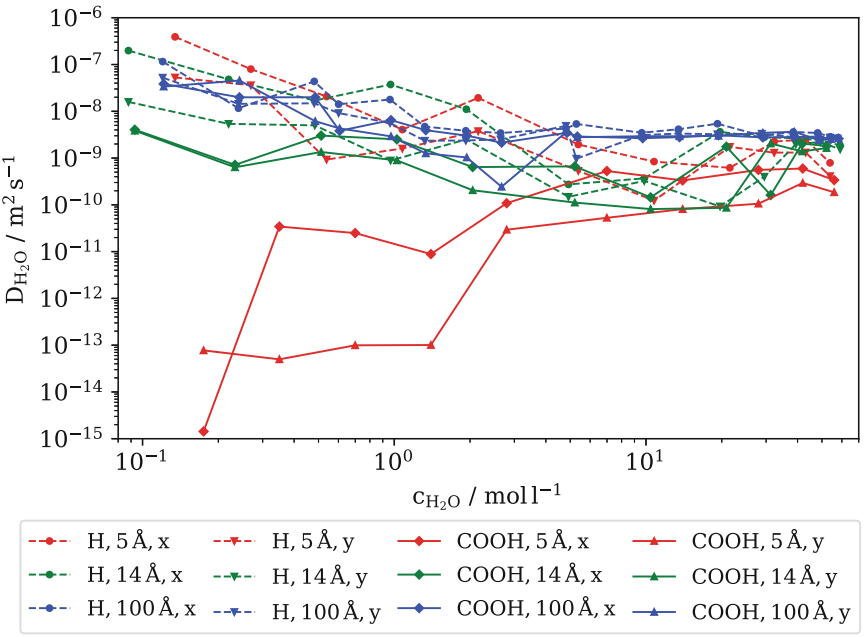


Fig. 7.5 Computed self-diffusion constants of water in the slit pores in the directions parallel to the graphite slab surface with unfunctionalised (C–H) and functionalised (additional –COOH groups) termination

where $\mathbf{r}_i(0)$ and $\mathbf{r}_i(t)$ are the particle positions at the time origin and at time t, respectively, plotted over t. Multiple time origins are used to improve statistics. Self-diffusion constants in the two directions parallel to the slab surface (x and y) were determined for the different slab geometries and water loadings (see Fig. 7.5). An anisotropy in the diffusivity can be observed especially for lower loading, due to the different corrugation of the surface in the two surface orientations, which can be traced back to the layered nature of graphite. As expected, the speed of diffusion is reduced for smaller pore sizes and generally decays towards high water concentrations, except for the COOH-functionalised 5 Å pore, where the diffusivity at lower concentrations is reduced by several orders of magnitude. Here, the strong interaction of the guest molecules with the pore walls significantly reduces their mobility. This effect is also observable in the 14 Å pore, albeit to a much lesser degree. Thus, in smaller pore size regimes of functionalised char, host-guest interactions increasingly dominate the diffusive behaviour of adsorbed water.

7.3 Reactive Processes

Previous investigations of elementary reaction steps for the combustion of solid fuels have mostly been limited to pyrolysis and primarily concerned with the unimolecular decomposition of small functionalised aromatic hydrocarbons [20–22].

UNCORRECTED

Author Proof

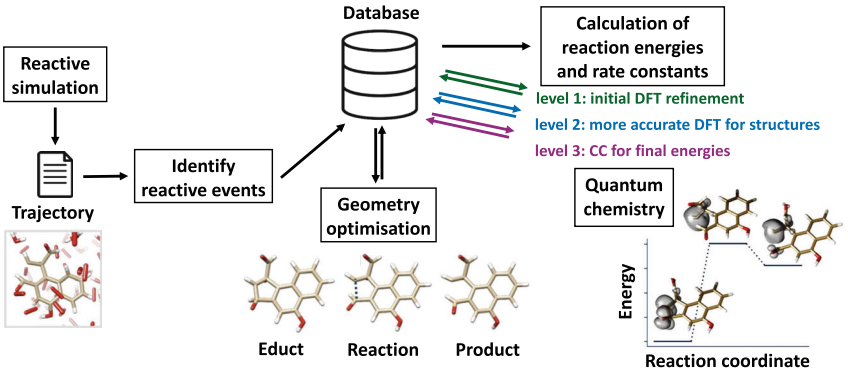


Fig. 7.6 Workflow for the automatised reaction discovery and refinement

In difference to pyrolytic conversion, combustion comprises a large variety of reactions with oxygen-containing radical species. Accurate detailed mechanisms at the level of elementary reactions are only available for a number of liquid and gaseous fuels [23–26].

In the current study, elementary reaction steps for the oxidation of molecular surrogates for char were investigated with a workflow that makes use of several methods, each specialised for a particular task.

7.3.1 Multi-Method Approach for Reaction Networks and Rate Coefficients

The chemical space of combustion of even small char surrogate models is vastly huge and automatic tools for reaction discovery are indispensable for the exploration of the reaction network. There are various options for reaction sampling techniques. An approach was chosen which utilises reactive MD simulations with cost-effective methods like ReaxFF and GFN-xTB. This allows to sample the potential energy surface and to discover key reactions.

These methods alone are, however, not sufficient: The amount of reaction events makes it infeasible to analyse them by hand. Furthermore, the limited accuracy of ReaxFF or GFN-xTB does not allow for quantitative predictions. Both issues are addressed by introducing an automated workflow from MD simulations to accurate quantum chemical calculations [27] sketched in Fig. 7.6. In a first step, relevant reactions are identified and filtered to remove redundancies during the reactive simulation by comparing to previously detected reactions already stored in a database.

In the second step these reactions are post-processed on higher levels of theory, which allows to target quantitative predictions. The treatment on various levels of theory allows to employ accurate, but computationally costly electronic structure methods only for those reactions, which before on a lower level of theory were found to be most likely relevant.

UNCORRECTED PR

Author Proof

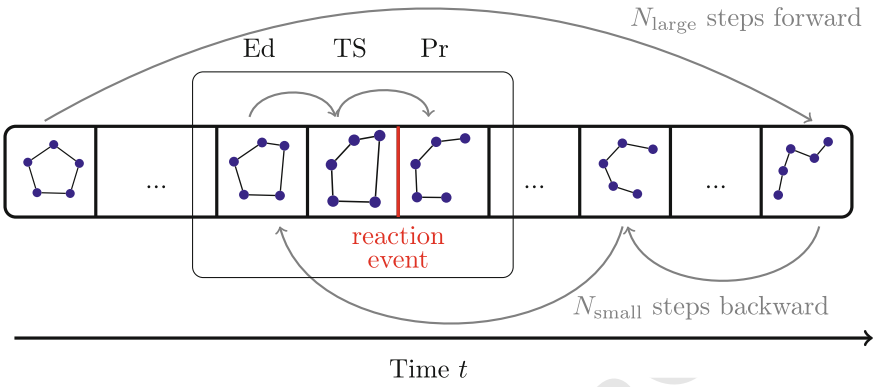


Fig. 7.7 Illustration of the trajectory scan. If a reaction event is found three frames for the educt (Ed), transition state (TS) and product (Pr) are stored for post-processing

For each start system, usually 5 MD simulations with different random start velocities are run and the trajectories stored in a portable HDF5 file. After completion of the simulation, the reactions are identified as bond breaking or formation events and extracted from the trajectory in the HDF5 file. For this, the structures for each time step of the MD simulation are mapped onto an (undirected) molecular graph. The connectivity for the graph stems from bond orders. A bond order larger 0.5 is used as criterium for a bond between two atoms to determine the connectivity of the molecular structure and thus the graph. The graph representation is used to compare the frames within a trajectory and thereby locate reactive events. For efficiency reasons this search is not done frame by frame but, as illustrated in Fig. 7.7, the frame index is incremented by a user-defined step size N_{large} (default 200). If a change in a molecular graph is detected, the search direction is reversed employing a smaller step size N_{small} (default 10), which will be reduced down to 1 to locate the frames, where the reaction event took place. If a reaction event was found, three frames representing the educt(S), product(S), and the transition state, are stored for post-processing. It is distinguished between unimolecular rearrangements and non-unimolecular reactions involving either on the educt or product side more than one species.

Table 7.2 Statistics of filtered reactions [27]. Listed are the total number of located reactions n_r and the number of unique reactions $n_{\bar{r}}$. Additionally the number of unique reactions in which the molecular C-graph changes $n_{\bar{r}}^{(C)}$ and the screening ratio $Screen = (n_r - n_{\bar{r}})/n_r$ are given

	$C_{16}H_9$					$C_{20}H_{11}$				
run	1	2	3	4	5	1	2	3	4	5
n_r	1643	2494	1166	809	978	3829	3733	50	498	3933
$n_{\bar{r}}$	103	32	11	34	14	11	8	9	41	7
$n_{\bar{r}}^{(C)}$	38	10	3	8	4	2	2	20	1	0
$Screen/\%$	94	99	99	96	99	99.9	99.9	82	92	99.9

UNCORRECTED PROOF

Author Proof

For an efficient analysis, it is vital to filter the found reactions to extract a set of relevant unique reaction events. This filtering process is also done on the basis of the graph representation. In addition Cartesian coordinates are stored to distinguish stereo isomers. During the comparison, it is tracked if the molecular species belong to the educt or product side for the classification as forward or backward reaction. If a reaction r is not found in the database it is added as new unique reaction. The first reaction of its kind is always classified as forward reaction. Table 7.2 highlights the importance of the filtering process, as screening ratios up to 90 % have been observed.

Reaction and Activation Energies

After the reaction discovery, the structures of educts, products, and transition states of the newly identified unique reactions are in a first step refined at the DFT level using a computationally cheap meta-GGA functional and a small basis set, TPSS-D3/SVP. Depending on the method used in the reaction discovery step, only information on the molecular geometries and possibly charges are available from the latter. However, additional information is needed to unambigously specify the electronic states of the reactants when the electronic structure is taken into account. This includes in addition to the charges the information on the spin state: at the DFT level the Z component of the electronic spin, M_S, which sets a lower bound for the spin quantum number $S \geq |M_S|$ and the number of unpaired electrons. To determine M_S, a single-point DFT calculation with Fermi smearing [27,28] is done. After the Fermi smearing calculation, fractional occupation numbers are rounded to the closest integer and an initial value for M_S is determined as $M_S^{\text{init}} = (n_\alpha - n_\beta)/2$. The DFT energy without Fermi smearing is then evaluated for M_S^{init}, and, where possible, for $M_S^{\text{init}} \pm 1$. The spin orbital occupations resulting in the lowest DFT energies are then used for the subsequent calculations.

Next, the geometries of the reactants are optimised at the DFT/TPSS-D3/SVP level and the molecular graphs of the optimised structures are compared with the initial graphs from the reaction discovery. If the molecular graphs changed, the further refinement is skipped because the respective reaction has then no counterpart on the DFT potential energy surface.

To ensure that along a reaction the spin states of the educts, the transition state, and the products are compatible also for non-unimolecular cases, e.g. $\mathrm{A} + \mathrm{B} \longrightarrow [\mathrm{TS}] \longrightarrow \mathrm{C} + \mathrm{D}$, for the educts and for the products the sets of possible total M_S values, M_S^{educts} and M_S^{products}, respectively, is determined that can be reached by coupling of the individual spins. Only values contained in both sets and, thus, compatible with a spin-conserving reaction, are considered. In the workflow for the location of transition states on the DFT potential energy surface (PES) there is the possibility to either refine the structure from the MD trajectory using an algorithm for the optimisation for saddle points or, if this fails, to use a double ended reaction pathway optimisation. If the sets of possible values of M_S for the educts and products do not contain a common value, the workflow tries to optimise the transition state structure starting from the initial guess found during the reaction discovery with all values for M_S possible for the assumed products or the assumed educts. The final educts

UNCORRECTED PROOF

Author Proof

and products of the reaction on the DFT PES are then determined from the DFT transition state by following the reaction coordinate (gradient extremal) pathways downwards in forward and backward direction.

As mentioned above, the workflow uses two alternative algorithms to locate transition states. The first one is partially adopted from the studies by Döntgen et al. [29,30] and Kröger et al. [31]. It starts from the structures identified during the reaction discovery step as those where a bond breaking or formation event is happening (see above). These structures are first preoptimised at the DFT level with fixed bond distances for the „reacting" bonds to bring all other coordinates close to equilibrium. Then the Hessian for the nuclear coordinates is calculated for this pre-optimised structure and a regular saddle point optimisation with a trust-region image minimisation algorithm is carried out.

In any case, it is verified by a final Hessian calculation that transition states are first-order saddle points. Forward and backward intrinsic reaction coordinate calculations are used to verify the educts and products that are connected by the located transition state. For non-unimolecular reactions where the IRCs end at structures with (weakly interacting) separate reactants, the spin orbitals are localised and assigned to the individual fragments which allows to identify the individual M_S spin quantum numbers. Then, the geometries of the separate fragments are optimised. The molecular graphs of the optimised IRC end points and the respective values for M_S are compared to those of the assumed reference educts and products that were obtained from the refinement of the structures identified in the reaction discovery. If they do not agree, the results are assigned to a new reaction and a second algorithm to locate the correct transition state for the searched-for reaction is used which starts with a double-ended reaction path optimisation between the DFT-optimised educt and product structures.

For those reactions that could successfully refined with the low-accuracy DFT method, the geometries of the reactants and the transition states are further refined with the more accurate meta-GGA hybrid functional TPSSh-D3 and the more accurate, larger TZVP basis. The same level of theory, DFT/TZVP-D3/TZVP is also used to compute within the harmonic approximation the vibrational frequencies for the zero-point vibrational energy contributions and for the calculation of the partition functions.

While DFT/TZVP-D3/TZVP gives structures and harmonic vibrational energies that are sufficiently accurate for the purposes of this work, the electronic energies obtained at this level of theory are not sufficient for the requirements on reaction energies and rate coefficients. Therefore, in the last step of the refinement workflow accurate electronic energies at the DFT-optimised structures are computed for the reactants and transition states. For this, the explicitly correlated coupled-cluster singles-and-doubles method is employed with a scaled perturbative triples corrections, CCSD(F12*)(T*), with optimised basis set for this level, cc-pVDZ-F12. For open-shell systems, the CCSD(F12*)(T*) calculations are done based on restricted open-shell Hartree-Fock (ROHF) reference wavefunctions to avoid that the accuracy of the results is impaired by spin-contamination.

UNCORRECTED PROOF

Author Proof

Rate Coefficients

The rate coefficients are calculated within the framework of transition state theory with transmission coefficients evaluated in the high temperature limit of the Eckart tunneling correction. The partition functions needed for this are calculated within a modified qRRHO approximation [9,10]. The rate coefficients are temperature dependent, most importantly through an exponential factor depending on the activation barrier. For a compact representation of the rate coefficients $k(T)$ over a wide temperature range, parameters A, n, and E for a modified Arrhenius expression

$$k(T) = A\,T^n \exp\left(-\frac{E}{T}\right) \tag{7.2}$$

are fitted with a non-linear least-square fit to explicitly computed rate coefficients on a grid for the temperature range 300–3000 K.

7.3.2 Reaction Discovery with Reactive MD

The performance of reaction MD simulations for polyaromatic hydrocarbons in an oxy-fuel atmosphere in terms of the required simulation length and the outcome is mostly determined by the concentration of radicals that can initiate combustion reactions and the simulated temperature. In reactive MD simulations at physical combustion temperatures of $\approx$ 1000 K, O_2 reacts only very rarely with hydrocarbons without radical centres. Usually, aryl and oxo (RO·) radicals are formed in the first steps of hydrocarbon combustion. These radicals are much more reactive and, thus, are efficient starting points for reactive MD simulations.

In early ReaxFF studies on char combustion [7], large coal models were oxidised at high temperatures of 3000–4000 K for 250 ps to resolve the bottleneck for the initial reaction steps. However, applying simulation temperatures higher than 3000 K causes an unphysical bias towards pyrolytic cracking reactions. The oxidation of perylene ($C_{20}H_{12}$) is investigated in two distinct combustion atmospheres at 2000 and 4000 K (Table 7.3). At 4000 K and in the absence of radical species, perylene undergoes rapid fragmentation into different C_2–C_7 gas-phase species before these fragments are oxidised by molecular oxygen. For example, after 0.1 ns two acetylene fragments were eliminated which were subsequently oxidised by O_2 to carbon dioxide. In fact, the unimolecular fragmentation reactions are similar to pyrolytic cracking and do not involve radicals or molecular oxygen in the combustion atmosphere. At lower temperatures (2000 K) perylene is nonreactive and no oxidation event was detected even after 10 ns. Only if in addition hydroxyl radicals are added to the atmosphere, perylene is oxidised rapidly at both simulation temperatures. But even with HO· present fragmentation reactions involving dehydrogenation and acetylene or ethene elimination reactions are at 4000 K the main initial reaction channels that lead to the decomposition of the aromatic system. Hence, radical species are crucial for an efficient but realistic simulation of combustion reactions of PAHs and open up different reaction channels involving molecular oxygen. These open-shell gas-phase

UNCORRECTED PROOF

Author Proof

Table 7.3 The influence of radical species and temperature in ReaxFF simulations using perylene as a typical PAH system

Temperature	Radicals	Oxygen	Observation
2000 K	None	40 O_2	Nonreactive
4000 K	None	40 O_2	Fragmentation (after 0.1 ns)
2000 K	10 OH radicals	40 O_2	Edge carbon oxidation
4000 K	10 OH radicals	40 O_2	Fragmentation (after 0.1 ns)

no index

molecules trigger oxidation reactions, e.g. by abstracting hydrogen atoms from the edge of a PAH system, thereby forming intermediate aryl radicals.

To minimise a potential bias of simulations caused by unreasonably high radical concentrations in the simulation box, a preprocessing tool for generating transition states for the radical initiation reactions is implemented. The hydrogen abstraction transition state explorer (HyATraX) [32] can be used as a tool to generate reactive intermediates that are generated via common initial reaction channels involving hydrogen atoms or hydroxyl radicals. The formation of these aryl radicals is time consuming during the MD simulations at physically reasonable temperatures ($\lessapprox$ 2000 K). Also PAHs with heteroatomic functional groups also tend to be non-reactive in the absence of gas-phase radical species in the atmosphere and do not solve this problem. The application of HyATraX facilitates the quick generation of open-shell intermediates and the automatised calculations of the respective activation and reaction energies which are depicted schematically in Fig. 7.8 for two selected nitrogen-containing PAHs. The generated radical intermediates can be used as an input for MD simulations, thereby reducing the computational time by lifting the bottleneck of the slow initial abstraction reactions. The analysis of multiple trajectories with different randomly chosen starting velocities leads to a reaction network that can be further expanded by sampling additional trajectories for stable intermediate structures. This allows different combustion products to be linked and more complete reaction networks to be created. Also in general it is important for the completeness of the reaction network that enough trajectories with different start conditions are generated. While for oxygen- and sulphur-containing PAHs it was found that five individual runs are sufficient to explore the reaction space of these systems, this changes when nitrogen is included in the carbon framework. Nitrogen stays carbon-bound during the oxidation reactions and forms NO_x precursors, whereas oxygen and sulphur functionalities are eliminated in the initial reaction steps. It turned out that typically about 15 MD runs are needed to cover the reaction network for nitrogen-containing PAHs.

As alternative to reactive force fields, semi-empirical xTB methods can be applied for the reaction discovery. Specifically for char models containing potassium and other alkali metal atoms for which currently no ReaxFF parametrisations suitable for combustion is available, GFN2-xTB is currently the only feasible option to sample the reaction space for combustion. GFN2-xTB is parameterised for almost the whole

UNCORRECTED PROOF

Author Proof

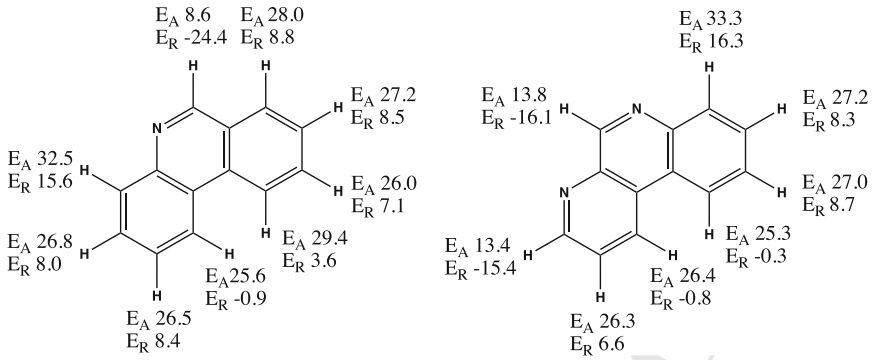


Fig. 7.8 Reaction energies (E_R) and activation barriers (E_A) in kJ mol^{-1} of initial hydrogen abstraction reactions by H atoms in two nitrogen containing PAHs. Transition states and products were generated with the HyATraX tool at the DFT/TPSS/TZVP level

periodic table and, in contrast to ReaxFF, does not require different parameterisations for different reaction conditions. In addition, it uses an electronic wavefunction which has some advantages for the transfer of the MD results to the DFT refinement. The price to be payed for this are the larger computational costs of GFN2-xTB simulations that are at least one order of magnitude higher than for ReaxFF.

paid

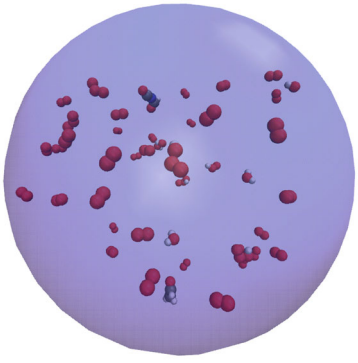
For the MD simulations with GFN2-xTB, a nanoreactor setup is employed, where the reactants are placed in a spherical confinement (Fig. 7.9). Furthermore, an artificial central force is applied which partially compensates for the increased computational complexity of GFN2-xTB by increasing the number of collisions and thus the reactivity of the system:

$$\mathbf{F} = \mathrm{sign}(\mathbf{r}_i - \mathbf{o})\, k_F\, m_i\, (\mathbf{r}_i - \mathbf{o})^2\,. \tag{7.3}$$

In (7.3), m_i denotes the mass of atom i, $\mathbf{r}_i$ its position vector and $\mathbf{o}$ the centre of the simulation box. Moreover, the force is defined by a predetermined force constant k_F. For the construction of the molecular graph, approximate bond orders are calculated

Fig. 7.9 Spherical confinement (blue) used in the GFN2-xTB MD simulations

too tight layout



UNCORRECTED PROOF

Author Proof

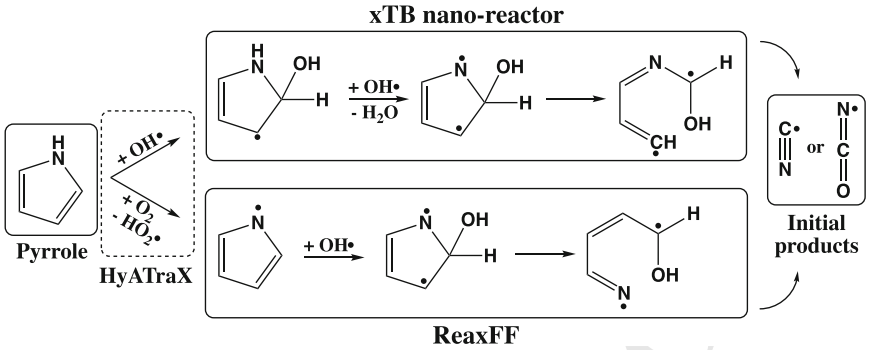


Fig. 7.10 Initial oxidation events of pyrrole in the xTB nanoreactor and ReaxFF simulations. The MD simulation of the hydrogen abstraction reaction can be skipped by applying HyATraX

as [33]:

$$\xi(r_{i,j}) = \frac{1}{1 + \exp\left[-k_1\left(k_2\left(R_{i,\mathrm{cov}} + R_{j,\mathrm{cov}}\right)/r_{ij}\right) - 1\right]}, \tag{7.4}$$

where $R_{i,\mathrm{cov}}$ are pre-tabulated covalent radii and $k_1 = 16$ and $k_2 = 4/3$.

The agreement between the initial reaction products and reaction mechanisms in both approaches is confirmed by a direct comparison of the reaction events observed in the ReaxFF simulations and GFN2-xTB nanoreactors. A suitable example of the initial reactions of pyrrole in an oxygen atmosphere containing hydroxyl radicals in both setups is provided in Fig. 7.10.

Pyrrole reacts in both simulations to cyanides and isocyanates. The first step is the abstraction of hydrogen atoms from the aromatic system that can be directly generated with HyATraX. Thereafter, hydroxyl radicals add to the carbon framework before the heterocycle breaks apart and reacts with additional radicals in the combustion atmosphere. Besides, the nanoreactor setup leads to the same initial products as observed in the ReaxFF simulations.

7.3.3 Initial Reactions and Influence of Functional Groups

With increasing temperature during combustion, radical species open up new reaction channels leading to reactive intermediates that increase the reactivity of char subsystems. Next to the initially generated radicals, small volatile reactive species are eliminated from the carbon framework in the later stages of the combustion process, e.g. formic acid, formaldehyde, their analogue radicals, carbon monoxide and carbon dioxide. At the beginning of char combustion, the abstraction of hydrogen atoms from aromatic C–H bonds is one of the most important initiation reaction channels during combustion. The abstraction of individual hydrogen atoms from the edge of PAHs leads to the formation of aryl radicals as highly reactive species that can react with species in the combustion atmosphere including O_2. The molecular composition and quantity of highly structured and amorphous PAH-areas in (bio)chars is

UNCORRECTED PROOF

Author Proof

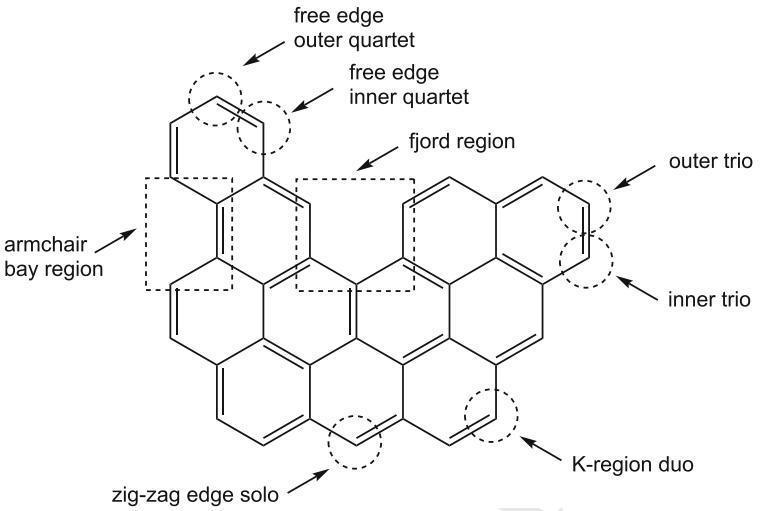


Fig. 7.11 Nomenclature of reaction sites in a generalised PAH

a non-uniquely defined and feedstock-dependent property. Their reactivity can not be modelled at the atomistic level with just a single molecular surrogate. In general, they contain polyaromatic substructures with different shapes and sizes offering individual reaction sites of which the most important ones are schematically depicted in Fig. 7.11.

To account for the diversity in reaction sites for the hydrogen abstraction by atomic hydrogen, Yönder et al. [9] calculated temperature-depended reaction rate coefficients for PAHs with different sizes and reported generalised site-specific kinetic parameters for hydrogen abstraction reactions at the CCSD(F12*)(T*) level (Table 7.4) that allow to extrapolate the kinetic data to differently sized and shaped PAHs.

Beside interlinked aromatic and aliphatic hydrocarbons, char contains mostly oxygen, nitrogen, and sulphur functional groups that can enhance its reactivity by allowing for reaction channels with lower activation barriers. During combustion,

Table 7.4 Non-linear least-square fit of the calculated rate coefficients k to a modified Arrhenius equation (see (7.2)) for studied reaction sites [9]

Site type	A/cm^3 mol^{-1} s^{-1}	N /-	E/K
Zigzag edge solo	1.25×10^8	1.76	7585
K-region duo	1.30×10^8	1.78	7437
Inner trio	1.82×10^8	1.76	7469
Outer trio	1.27×10^8	1.80	7333
Free edge inner quartet	1.17×10^8	1.81	7361
Free edge outer quartet	1.20×10^8	1.82	7319
Armchair bay region	9.26×10^7	1.75	7468

UNCORRECTED PROOF

609647_1_En_7_Chapter-online ☑ TYPESET ☐ DISK ☐ LE ☑ CP Disp.:20/9/2025 Pages: xxx Layout: German_T1

Author Proof

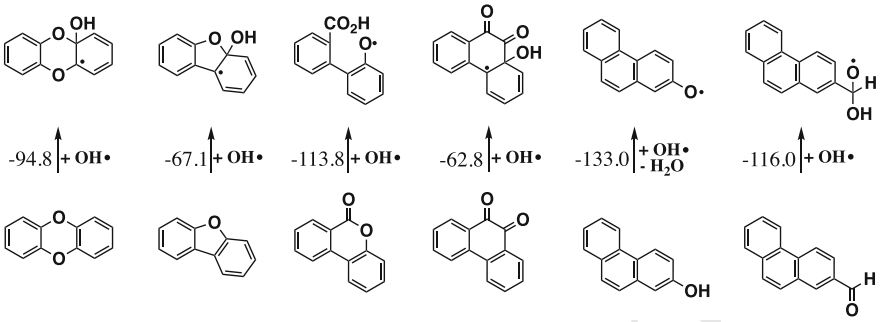


Fig. 7.12 Barrierless initial reactions of OFGs with hydroxyl radicals leading to reactive open-shell oxo-intermediates shown with the corresponding reaction energies (kJ mol^{-1}) at CCSD(F12*)(T*)/cc-pVDZ-F12 level. From left to right: dioxine, furan, lactone, dicarbonyls, aromatic alcohols, and aldehydes [34]

aldehydes, carboxylic acids, aromatic alcohols, quinones, furans, and dioxins can react exothermically with hydroxyl radicals (OH·) without significant barriers, forming reactive open-shell intermediates.

Figure 7.12 shows an overview of initial hydroxyl radical addition reactions in phenanthrene-sized systems with oxygen-containing functional groups (OFGs) together with the reaction energies. The generated radical species can react further with molecular oxygen (O_2) or peroxyl radicals (HO_2·) to create highly oxidised intermediates initiating the break-down of the carbon framework.

Carboxylic acids (COOH), for example, tend to undergo decarboxylation after the hydrogen atom from the acid functionality has been abstracted by a hydroxyl radical. The generated aryl radical reacts with molecular oxygen, opening reaction

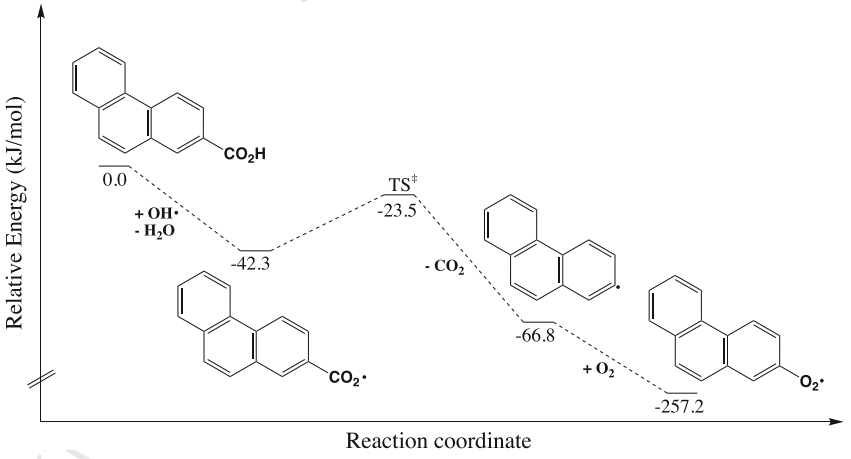


Fig. 7.13 Reaction energies (kJ mol^{-1}) at the CCSD(F12*)(T*)/cc-pVDZ-F12 level for the decarboxylation phenanthrene-2-carboxylic acid and the subsequent addition of O_2. Energies are relative to the reactants [34]

609647_1_En_7_Chapter-online ☑ TYPESET ☐ DISK ☐ LE ☑ CP Disp.:20/9/2025 Pages: xxx Layout: German_T1

Author Proof

channels for radical chain branching reactions. This reaction type was observed, e.g. for phenanthrene-2-carboxylic acid (Fig. 7.13). The decarboxylation has a comparatively small activation barrier of 18.8 kJ mol^{-1} with a reaction energy of −24.5 kJ mol^{-1}. The addition of dioxygen (O_2) to the resulting aryl radical is barrierless and highly exothermic releasing an energy of −190.4 kJ mol^{-1} (cf. Fig. 7.13).

abundant

The most abundand sulphur functional groups (SFGs) in char are thiophenes, thiols (R–SH), sulphonic acids (R–SO_3H), thioketones ($R_2C = S$), and cyclic sulphones (R − −SO_2-R). Terminal SFGs are oxidised during combustion, e.g. by hydroxyl radicals step-wise to sulphenic, sulphoxylic, and sulphonic acids before they are eliminated as the H_ySO_x gas-phase species (compare Fig. 7.14) [35]. In thiophenes the sulphur atom is part of the aromatic ring system and, thus, reacts differently in the initial reaction steps compared to terminal SFGs. Thiophene itself reacts e.g. with hydroxyl radicals that add to the aromatic ring system before a C–S bond is broken. The generated thiyl radical can then recombine with different radicals present in the combustion atmosphere, e.g. a second hydroxyl radical. At this step, sulphur can eliminate as a thioperoxyl radical (SOH). Embedded thiophenes react slightly differently: For these species, sulphur tends to leave the aromatic framework via elimination of carbonyl sulphide (COS), the mono-sulphur analogue of carbon dioxide.

The most common nitrogen functional groups (NFGs) in char are pyrroles, pyridines, and diketopiperazine groups. Different initial radical sites generated with the HyATraX [32] tool revealed large variations in reactivities. While, e.g. pyrrole 1-yl did not react further during the course of the ReaxFF simulations, the 2-yl and 3-yl radicals exhibit high reactivity and are oxidised rapidly by molecular oxygen or hydroxyl radicals. Typically nitrogen tends to stay carbon-bonded during the initial oxidation reactions until the NFGs are converted into NO_x precursors like hydrogen cyanide (HCN), methanimine (H_2CNH) or (iso)cyanates (NCO, CNO). Heterocyclic N-compounds either undergo hydrogen abstraction reactions or direct oxidation, e.g. by hydroxyl radicals from the combustion environment. Addition-

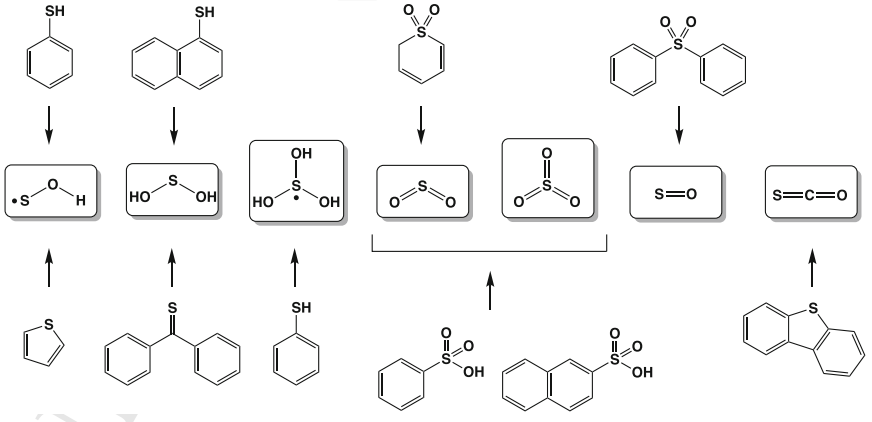


Fig. 7.14 Initial H_ySO_x elimination products of different sulphur functional groups (SFGs) in varying system sizes observed in ReaxFF

Author Proof

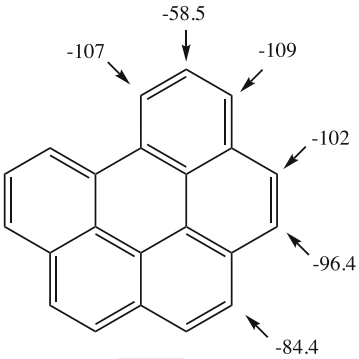


Fig. 7.15 Reaction energies (kJ mol^{-1}) for the addition of atomic oxygen at different reaction sites in benzo[ghi]perylene [36]

ally, C–C or C–N bond dissociations lead to fragmentation and further elimination reactions, e.g. the formation of formaldehyde and different NO_x precursors. Non-aromatic diketopiperazines react similarly forming cyanides and primarily ketenes as initial elimination products. The NO_x precursors then react with atomic and molecular oxygen to nitrogen monoxide (NO) and dioxide (NO_2).

7.3.4 Break-Down of the Carbon Framework

After terminal functional groups have eliminated or induced ring-opening reactions the carbon framework is gradually decomposed by the oxygen species present in the combustion atmosphere. One important reaction channel that initiates the break-down of aromatic carbon frameworks involves the addition of molecular (Eq. (7.5)) or atomic oxygen (Eq. (7.6)) to the hydrocarbon system, forming highly reactive oxyradicals. Aryl radicals (C_xH_{y-1}) reacts with molecular oxygen forming oxyl radicals ($C_xH_{y-1}O$) and highly reactive atomic oxygen:

$$C_xH_{y-1} + O_2 \rightarrow C_xH_{y\text{-}1}O_2 \rightarrow C_xH_{y\text{-}1}O + O(^3P) \tag{7.5}$$

Atomic oxygen ($O(^3P)$) can add aromatic rings which then rearrange, e.g. by eliminating atomic hydrogen to oxyl radicals:

$$C_xH_y + O \rightarrow C_xH_yO \rightarrow C_xH_{y\text{-}1}O + H\cdot \tag{7.6}$$

Figure 7.15 shows for example the reaction energies for the $O(^3P)$ addition at different sites in benzo[ghi]perylene.

The aryl oxyl radicals can subsequently eliminate CO [36] leaving behind a reactive radical that can react further, e.g. with molecular oxygen. The CO elimination can occur in a single-step, as observed in pentacene, or through a multi-step pathway via additional intermediates as observed for anthanthrene. The mechanistic details for the elimination reaction are influenced by geometric strain and steric effects at the various reaction sites in specific PAHs. The geometrical effects significantly influence the activation energies of the CO elimination. Due to geometrical strain,

UNCORRECTED PROOF

Author Proof

Table 7.5 Activation energy ranges in kJ mol^{-1} for CO elimination at different site types in PAHs [36]

Site type	$\Delta E^{\ddagger}$/kJ mol^{-1}
Outer trio	140–162
Outer quartet	170–194
Duo & 2 neighbours	182–220
Inner quartet	189–242
Inner trio	240–257
Solo	304–380

so-called solo sites located in the centre of edges generally exhibit the highest activation barriers for CO elimination reactions. Table 7.5 lists an overview of activation energies for the time-determining step of the CO elimination.

Oxygen functional groups (OFGs) are contributing to the decomposition of the carbon backbone by increasing the local reactivity. The attack of different radicals onto the carbon framework can lead to a distortion of the aromaticity. Commonly, the oxidation of two adjacent carbon atoms initiates a C–C bond dissociation which then either opens a ring or causes the elimination of a volatile fragment. Figure 7.16 shows typical ring opening and contraction reactions for aromatic system with oxygen functionalities. These reactions generate functional groups which react easily further with molecular oxygen or different radicals and eliminate CO or CO_2. Also, nitrogen functional groups (NFGs) facilitate the decomposition of aromatic carbon frameworks. Nitrogen tends to stay carbon-bound throughout the char burnout process and leads to the formation of NO_x precursors that still contain carbon atoms as, e.g. CH_2NH, HCN, or CNO.

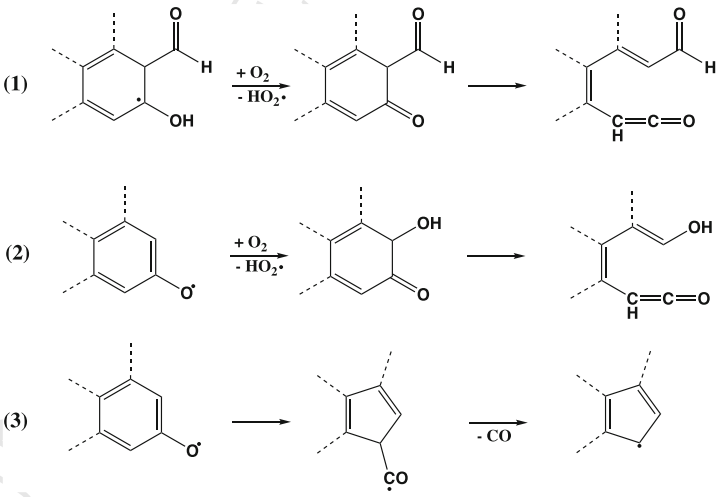


Fig. 7.16 Ring opening (1,2) and contraction (3) reactions during char burnout involving radicals from the combustion atmosphere

609647_1_En_7_Chapter-online ☑ TYPESET ☐ DISK ☐ LE ☑ CP Disp.:20/9/2025 Pages: xxx Layout: German_T1

Author Proof

7.4 Conclusion

During the last two decades, the theoretical modelling of char combustion at the atomistic level has made enormous progress on all scales from the electronic structure up to the dynamics of diffusion. The combination of tools specialised for different tasks on the various scales allows to study the processes involved in combustion, not only with less assumptions and less harsh approximations, but also more systematically and with higher accuracy.

Advanced computational tools have been used to establish an improved workflow to generate realistic char models. Since char consists mainly of graphitic carbon with a certain stacking of planes, but at the same time having a high defect ratio, a computational workflow is needed. This protocol has to adhere to the experimental boundary conditions like flake size or stack height, but should on the other hand not be restricted to artificial combinations of ideal graphene-like flakes. This was achieved by combining different methods and annealing steps. In addition, atomistic simulations for idealised model environments, like functionalised graphene slit pores, give access to transport properties of volatiles in pressure and temperature ranges inaccessible by experiment.

For an efficient, automatised and as much as possible unbiased reaction discovery, reactive MD simulations with ReaxFF and GFN-xTB were combined with an automatised generation of initial radical sites. This allowed to use more realistic temperatures and combustion atmospheres for the MD simulations than in previous studies and to avoid unphysical biases, e.g. towards fragmentation reactions because of unphysical high temperatures.

In general, the oxidation of the char model compounds can be divided into initiation reactions that generate reactive radical sites aromatic ring structures, and subsequent reactions that break-down the ring structures and eventually oxidise the fragments to CO, CO_2, and H_2O. The initiation reactions, such as hydrogen abstraction from the edge of polyaromatic regions, have high barriers or require highly reactive gas-phase radical species like HO·, H, or O. The so activated structures can react with molecular oxygen and other gas species in ring-opening and contraction reactions releasing CO and CO_2. Heteroatoms and functional groups increase the reactivity of char by reducing the activation barriers for the initiation reactions. Nitrogen atoms tend to remain carbon-bound during the initial steps, forming NO_x precursors like CH_2NH_2 or HCN. In contrast, sulphur is predominantly eliminated as H_ySO_x species. Besides, it was found that carbonyl sulphide (COS) can be released from embedded thiophenes. Oxygen-containing groups primarily decompose under the release of carbon oxides.

The decomposition of the carbon backbone begins with the oxidation of edge carbon atoms and continues as gradual decomposition from the outer edge to the inner core of the hydrocarbon. At the atomistic level, a large variety of reaction channels, reaction sites, and a number of volatile reactive radical species is observed in the combustion atmosphere that contribute to the char conversion.

Overall, the electronic structure calculations and molecular dynamics simulations provide a detailed atomistic insight into elementary reaction steps and individual

UNCORRECTED PROOF

Author Proof

contributions to diffusion and sorption processes. This helps to improve the understanding of the physical and chemical processes important for the combustion of solid fuels.

With MD simulations it has been possible to complement experimental measurements (see Sect. 5.3.2) for diffusion and sorption processes in char to temperature and pressure regimes that are difficult to access experimentally. The detailed atomistic insight from the simulations can be used to validate for example the assumptions made in development of a pore structure dependent adsorption kinetic model (see Sect. 5.3.3).

Similarly, the DFT calculations for the oxidation reactions at char surrogate models provide insight into the reaction mechanisms that are often experimentally not accessible for complex materials like (bio)char. The level of detail achievable with such calculations for elementary reaction steps, implies that for complex solid fuels it is not possible to cover all potential reaction channels and predict 1:1 the outcome of experimental combustion studies. However, they can complement experimental studies by providing atomistic insight into the reaction mechanisms that are difficult to obtain or even inaccessible. Most importantly, they provide kinetic data that is based on defined molecular compositions and, thus, transferable between different solid fuels independent of their origins. Such data is necessary for implementing and parameterising comprehensive and seamless char conversion models like the CRECK-S models, discussed in Sect. 8.2.3.

Acknowledgements This work has been funded by the Deutsche Forschungsgemeinschaft (DFG, German Research Foundation)—215035359—SFB/TRR 129 'Oxyflame'. The authors are indebted to Vanessa Angenent, Özlem Yönder, and LisaWarczinski for their contributions to this work. The authors are also grateful to Kai Leonhard and the authors of ChemTraYzer for helpful discussions and access to their code.

References

1. Hasse, C. "Models for Coal Kinetics". *Reference Module in Chemistry, Molecular Sciences and Chemical Engineering*. Elsevier, 2015. https://doi.org/10.1016/B978-0-12-409547-2.11520-3
2. Tremel, A. and Spliethoff, H. "Gasification Kinetics During Entrained Flow Gasification – Part II: Intrinsic Char Reaction Rate and Surface Area Development". *Fuel* 107 (2013), 653–661. https://doi.org/10.1016/j.fuel.2012.10.053
3. Miller, J. A., Pilling, M. J. and Troe, J. "Unravelling Combustion Mechanisms Through a Quantitative Understanding of Elementary Reactions". *Proceedings of the Combustion Institute* 30.1 (2005), 43–88. https://doi.org/10.1016/j.proci.2004.08.281
4. Hurt, R. H. and Calo, J. M. "Semi-Global Intrinsic Kinetics for Char Combustion Modeling". *Combustion and Flame* 125 (2001), 1138–1149. https://doi.org/10.1016/S0010-2180(01)00234-6
5. Wang, D.-m., Xin, H.-h., Qi, X.-y., Dou, G.-l., Qi, G.-s. and Ma, L.-y. "Reaction Pathway of Coal Oxidation at Low Temperatures: A Model of Cyclic Chain Reactions and Kinetic Characteristics". *Combustion and Flame* 163 (2016), 447–460. https://doi.org/10.1016/j.combustflame.2015.10.019

UNCORRECTED PROOF

Author Proof

6. van Duin, A. C. T., Dasgupta, S., Lorant, F. and Goddard, W. A. "ReaxFF: A Reactive Force Field for Hydrocarbons". *The Journal of Physical Chemistry A* 105.41 (2001), 9396–9409. https://doi.org/10.1021/jp004368u
7. Castro-Marcano, F., Kamat, A. M., Russo, M. F., van Duin, A. C. T. and Mathews, J. P. "Combustion of an Illinois No. 6 Coal Char Simulated Using an Atomistic Char Representation and the ReaxFF Reactive Force Field". *Combustion and Flame* 159.3 (2012), 1272–1285. https://doi.org/10.1016/j.combustflame.2011.10.022
8. Huang, Y., Cannon, F. S., Watson, J. K., Reznik, B. and Mathews, J. P. "Activated Carbon Efficient Atomistic Model Construction that Depicts Experimentally-Determined Characteristics". *Carbon* 83 (2015), 1–14. https://doi.org/10.1016/j.carbon.2014.11.012
9. Yönder, Ö., Schmitz, G., Hättig, C., Schmid, R., Debiagi, P., Hasse, C., Locaspi, A. and Faravelli, T. "Can Small Polyaromatics Describe Their Larger Counterparts for Local Reactions? A Computational Study on the H-Abstraction Reaction by an H-Atom from Polyaromatics". *The Journal of Physical Chemistry A* 124.46 (2020), 9626–9637. https://doi.org/10.1021/acs.jpca.0c07133
10. Grimme, S. "Supramolecular Binding Thermodynamics by Dispersion-Corrected Density Functional Theory". *Chemistry* 18.32 (2012), 9955–9964. https://doi.org/10.1002/chem.201200497
11. Bannwarth, C., Ehlert, S. and Grimme, S. "GFN2-xTB-an Accurate and Broadly Parametrized Self-Consistent Tight-Binding Quantum Chemical Method with Multipole Electrostatics and Density-Dependent Dispersion Contributions". *Journal of Chemical Theory and Computation* 15.3 (2019), 1652–1671. https://doi.org/10.1021/acs.jctc.8b01176
12. Angenent, V., Oelert, D. and Schmid, R. "Towards Realistic Structural Char Models: Generation of Stacked Graphene-Like Layers Using Constrained Reactive Molecular Dynamics Simulations". *Fuel* 372 (2024), 132064. https://doi.org/10.1016/j.fuel.2024.132064
13. Martínez, L., Andrade, R., Birgin, E. G. and Martínez, J. M. "PACKMOL: A Package for Building Initial Configurations for Molecular Dynamics Simulations". *Journal of Computational Chemistry* 30.13 (2009), 2157–2164. https://doi.org/10.1002/jcc.21224
14. Rappe, A. K., Casewit, C. J., Colwell, K. S., Goddard, W. A. and Skiff, W. M. "UFF, a Full Periodic Table Force Field for Molecular Mechanics and Molecular Dynamics Simulations". *Journal of the American Chemical Society* 114.25 (1992), 10024–10035. https://doi.org/10.1021/ja00051a040
15. O'Boyle, N. M., Banck, M., James, C. A., Morley, C., Vandermeersch, T. and Hutchison, G. R. "Open Babel: An Open Chemical Toolbox". *Journal of cheminformatics* 3 (2011), 33. https://doi.org/10.1186/1758-2946-3-33
16. Rappe, A. K. and Goddard, W. A. "Charge Equilibration for Molecular Dynamics Simulations". *The Journal of Physical Chemistry* 95.8 (1991), 3358–3363. https://doi.org/10.1021/j100161a070
17. Eisenbach, T., Duarte, H. A., Wedler, C., Pflieger, C., Muhler, M. and Span, R. "Experimental Investigations on the Adsorptive Behavior of H_2O Vapor on HTC Char Particles". *14th International Conference on Applied Energy*. Bochum, Germany, 2022. https://doi.org/10.46855/energy-proceedings-10289
18. Pflieger, C., Eckhard, T., Schmitz, G., Angenent, V., Göckeler, M., Senneca, O., Schmid, R., Cerciello, F. and Muhler, M. "Thermicity of the Decomposition of Oxygen Functional Groups on Cellulose-Derived Chars". *ACS Omega* 7.51 (2022), 48606–48614. https://doi.org/10.1021/acsomega.2c07429
19. Wu, Y., Tepper, H. L. and Voth, G. A. "Flexible Simple Point-Charge Water Model with Improved Liquid-State Properties". *The Journal of Chemical Physics* 124.2 (2006), 024503. https://doi.org/10.1063/1.2136877
20. Pielsticker, S., Möller, G. H., Gövert, B., Kreitzberg, T., Hatzfeld, O., Yönder, Ö., Angenent, V., Hättig, C., Schmid, R. and Kneer, R. "Influence of Biomass Torrefaction Parameters on Fast Pyrolysis Products Under Flame-Equivalent Conditions". *Biomass and Bioenergy* 119 (2018), 392–410. https://doi.org/10.1016/j.biombioe.2018.08.014

UNCORRECTED PROOF

Author Proof

21. Ling, L.-X., Zhang, R.-G., Wang, B.-J. and Xie, K.-C. "Density Functional Theory Study on the Pyrolysis Mechanism of Thiophene in Coal". *Journal of Molecular Structure: THEOCHEM* 905.1-3 (2009), 8–12. https://doi.org/10.1016/j.theochem.2009.02.040
22. Jiang, B., Yu, C.-F., Yuan, L., Lu, K., Tao, W., Lin, H. and Zhou, Y. "Investigation on Oxidative Pyrolysis Characteristics of Bituminous Coal Through Thermal Analysis and Density Functional Theory". *Applied Energy* 349 (2023), 121680. https://doi.org/10.1016/j.apenergy.2023.121680
23. Stagni, A., Cavallotti, C., Arunthanayothin, S., Song, Y., Herbinet, O., Battin-Leclerc, F. and Faravelli, T. "An Experimental, Theoretical and Kinetic-Modeling Study of the Gas-Phase Oxidation of Ammonia". *Reaction Chemistry & Engineering* 5.4 (2020), 696–711. https://doi.org/10.1039/C9RE00429G
24. Huang, C., Zhao, Y., Roy, I. S., Chen, B., Hansen, N., Pitsch, H. and Leonhard, K. "Pathway Exploration in Low-Temperature Oxidation of a New-Generation Bio-Hybrid Fuel 1,3-Dioxane". *Proceedings of the Combustion Institute* 39.1 (2023), 385–393. https://doi.org/10.1016/j.proci.2022.09.057
25. Kopp, W. A., Huang, C., Zhao, Y., Yu, P., Schmalz, F., Krep, L. and Leonhard, K. "Automatic Potential Energy Surface Exploration by Accelerated Reactive Molecular Dynamics Simulations: From Pyrolysis to Oxidation Chemistry". *The Journal of Physical Chemistry A* 127.50 (2023), 10681–10692. https://doi.org/10.1021/acs.jpca.3c05253
26. Jacobs, S., Döntgen, M., Alquaity, A. B. S., Hesse, R., Kruse, S., Beeckmann, J., Kröger, L. C., Morsch, P., Leonhard, K., Pitsch, H. and Heufer, K. A. "A Comprehensive Experimental and Kinetic Modeling Study of the Combustion Chemistry of Diethoxymethane". *Energy & Fuels* 35.19 (2021), 16086–16100. https://doi.org/10.1021/acs.energyfuels.1c01988
27. Schmitz, G., Yönder, Ö., Schnieder, B., Schmid, R. and Hättig, C. "An Automatized Workflow from Molecular Dynamic Simulation to Quantum Chemical Methods to Identify Elementary Reactions and Compute Reaction Constants". *Journal of Computational Chemistry* 42.32 (2021), 2264–2282. https://doi.org/10.1002/jcc.26757
28. Kresse, G. and Furthmüller, J. "Efficiency of Ab-Initio Total Energy Calculations for Metals and Semiconductors Using a Plane-Wave Basis Set". *Computational Materials Science* 6.1 (1996), 15–50. https://doi.org/10.1016/0927-0256(96)00008-0
29. Döntgen, M., Przybylski-Freund, M.-D., Kröger, L. C., Kopp, W. A., Ismail, A. E. and Leonhard, K. "Automated Discovery of Reaction Pathways, Rate Constants, and Transition States Using Reactive Molecular Dynamics Simulations". *Journal of Chemical Theory and Computation* 11.6 (2015), 2517–2524. https://doi.org/10.1021/acs.jctc.5b00201
30. Döntgen, M., Schmalz, F., Kopp, W. A., Kröger, L. C. and Leonhard, K. "Automated Chemical Kinetic Modeling via Hybrid Reactive Molecular Dynamics and Quantum Chemistry Simulations". *Journal of Chemical Information and Modeling* 58.7 (2018), 1343–1355. https://doi.org/10.1021/acs.jcim.8b00078
31. Kröger, L. C., Kopp, W. A., Döntgen, M. and Leonhard, K. "Assessing Statistical Uncertainties of Rare Events in Reactive Molecular Dynamics Simulations". *Journal of Chemical Theory and Computation* 13.9 (2017), 3955–3960. https://doi.org/10.1021/acs.jctc.7b00524
32. Schnieder, B., Schmid, R. and Hättig, C. *HyATraX (Data set)*. 2024. https://doi.org/10.5281/zenodo.12526535
33. Grimme, S., Antony, J., Ehrlich, S. and Krieg, H. "A Consistent and Accurate Ab Initio Parametrization of Density Functional Dispersion Correction (DFT-D) for the 94 Elements H-Pu". *The Journal of Chemical Physics* 132.15 (2010), 154104. https://doi.org/10.1063/1.3382344
34. Yönder, Ö., Schmitz, G., Schmid, R., Schnieder, B. and Hättig, C. "A Computational Chemistry Study on the Evolution of Oxygen Functional Groups During Char Burnout". *Fuel* 365 (2024), 131217. https://doi.org/10.1016/j.fuel.2024.131217
35. Schnieder, B., Schmid, R. and Hättig, C. "Quantum Chemical Study on the Evolution of Sulfur Functional Groups During Char Burnout". *The Journal of Physical Chemistry A* (2025). https://doi.org/10.1021/acs.jpca.4c07973

UNCORRECTED PROOF

Author Proof

879 36. Yönder, Ö. and Hättig, C. "Density Functional Theory Study of CO Formation Through Reac-
880 tions of Polycyclic Aromatic Hydrocarbons with Atomic Oxygen ($O(^3P)$)". *Fuel* 241 (2019),
881 851–860. https://doi.org/10.1016/j.fuel.2018.12.047

UNCORRECTED PROOF

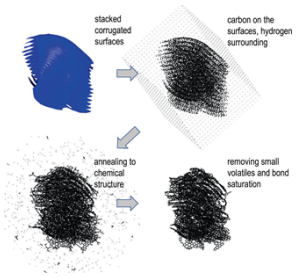
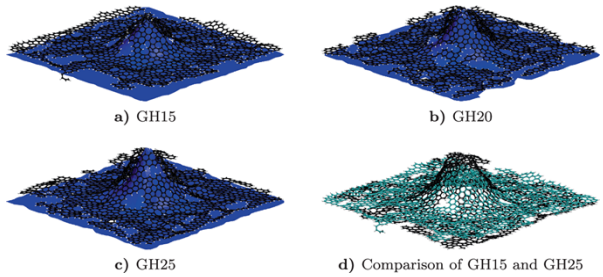
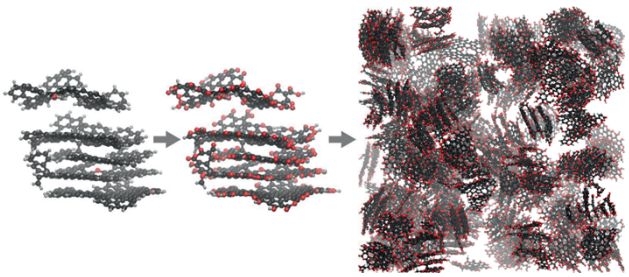
882 **Open Access** This book is licensed under the terms of the Creative Commons Attribution 4.0
883 International License (http://creativecommons.org/licenses/by/4.0/), which permits use, sharing,
884 adaptation, distribution and reproduction in any medium or format, as long as you give appropriate
885 credit to the original author(s) and the source, provide a link to the Creative Commons license and
886 indicate if changes were made.

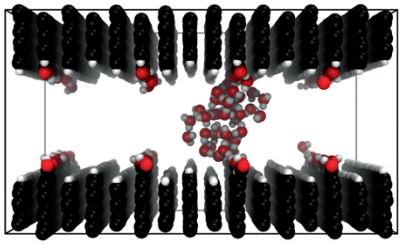
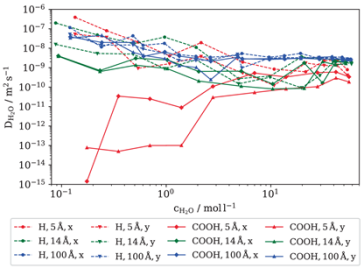
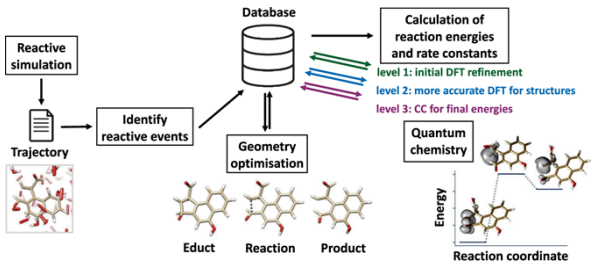
887 The images or other third party material in this book are included in the book's Creative
888 Commons license, unless indicated otherwise in a credit line to the material. If material is not
889 included in the book's Creative Commons license and your intended use is not permitted by
890 statutory regulation or exceeds the permitted use, you will need to obtain permission directly from
891 the copyright holder.

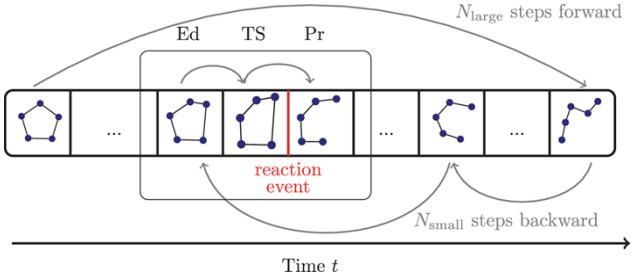
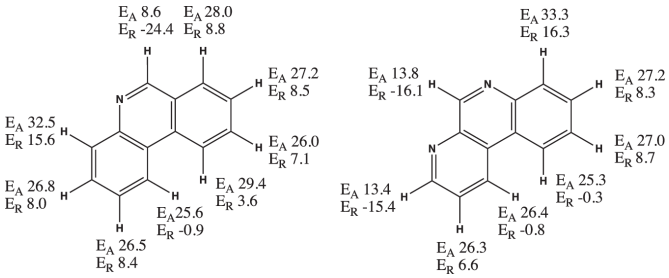
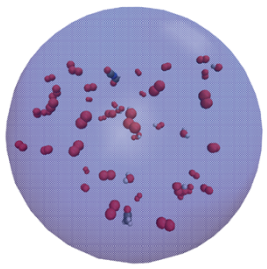
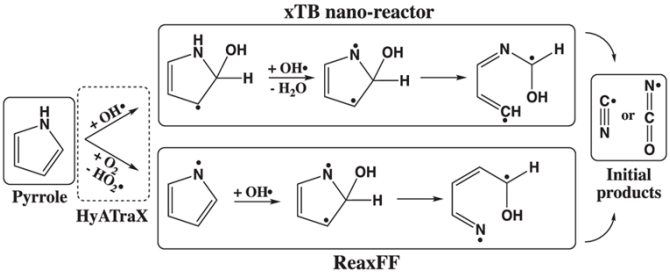
893

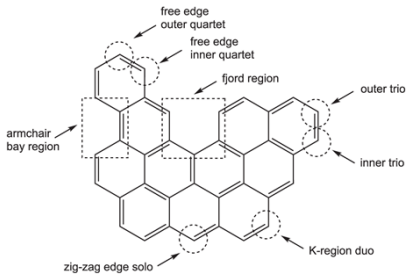
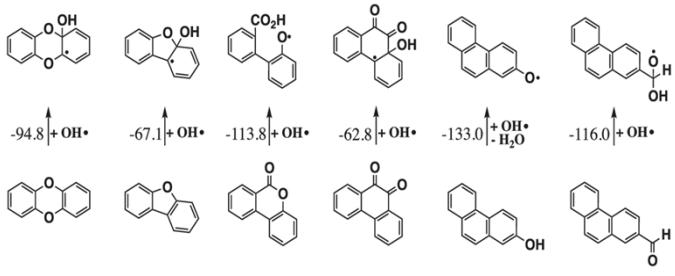
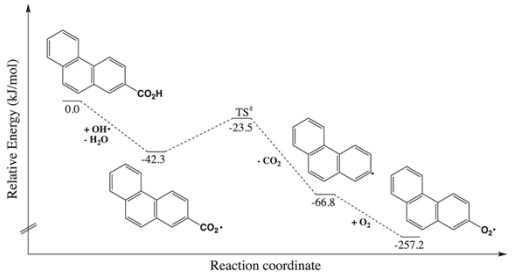
894 

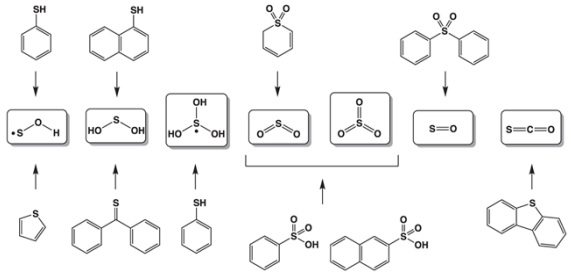
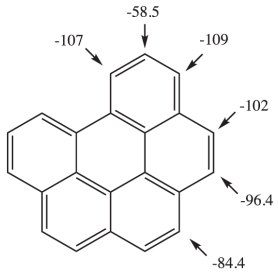
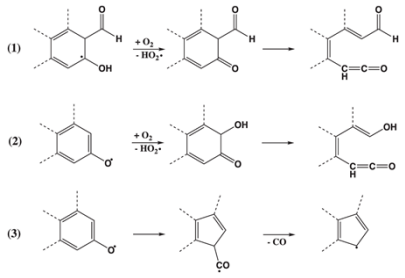
Alternative Texts for Your Images, Please Check and Correct them if Required

Page no	Fig/Photo	Thumbnail	Alt-text Description
6	Fig1		Diagram illustrating the transformation of stacked corrugated surfaces into a chemical structure. The process begins with blue stacked surfaces, transitioning to a black mesh-like structure labeled "carbon on the surfaces, hydrogen surrounding." Arrows indicate progression to "annealing to chemical structure," resulting in a denser black form. The final step, "removing small volatiles and bond saturation," shows a more compact structure.
8	Fig2		Four 3D plots labeled a) GH15, b) GH20, c) GH25, and d) Comparison of GH15 and GH25. Each plot displays a surface with varying elevations, represented in blue and green shades, indicating different data sets or conditions. The plots are arranged in a grid, with the comparison plot showing overlapping data for analysis.
8	Fig3		3D protein structure showing a sequence of conformational changes. The image depicts three stages: an initial compact form, an intermediate state, and a final complex structure. Each stage is represented by a network of interconnected atoms, with red and black spheres indicating different atomic elements. Arrows illustrate the transition between stages, highlighting the dynamic nature of the protein folding process.

Page no	Fig/Photo	Thumbnail	Alt-text Description
10	Fig4		3D plot depicting a molecular structure within a rectangular boundary. The structure consists of black, red, and white spheres representing different atoms, arranged in a layered pattern. The central area shows a cluster of red and white spheres, indicating a complex molecular interaction. The plot illustrates spatial relationships and molecular organization.
11	Fig5		Plot showing the diffusion coefficient of water (\(D_{H_2O}\)) in square meters per second against water concentration (\(c_{H_2O}\)) in moles per liter on a logarithmic scale. Multiple lines represent different conditions: hydrogen (H) and carboxyl (COOH) groups at varying distances (5 Å, 14 Å, 100 Å) and orientations (x, y). The legend differentiates these conditions with distinct colors and line styles.
12	Fig6		Flow chart illustrating a scientific process for analyzing chemical reactions. It begins with a "Reactive simulation" leading to "Identify reactive events" from a "Trajectory." This information is stored in a "Database" and undergoes "Geometry optimisation." The process involves "Calculation of reaction energies and rate constants" with three levels of refinement: "Initial DFT refinement," "More accurate DFT for structures," and "CC for final energies." The chart includes molecular structures labeled as "Edact," "Reaction," and "Product," and a graph titled "Quantum chemistry" showing energy changes over a reaction coordinate.

Page no	Fig/Photo	Thumbnail	Alt-text Description
13	Fig7		Flow chart illustrating a reaction process over time. The chart shows a sequence of molecular structures transitioning from an initial state (Ed) through a transition state (TS) to a product state (Pr). A red line marks the reaction event. Arrows indicate steps forward and backward, labeled as \(N_{\text{large}}\) steps forward and \(N_{\text{small}}\) steps backward. The timeline is denoted by "Time \(t\)" at the bottom.
18	Fig8		Chemical structure diagram showing two hexagonal ring compounds with various substituents. Each structure is labeled with values for \(E_A\) and \(E_R\) at different positions around the rings. The left structure has values such as \(E_A = 32.5\), \(E_R = 15.6\), and the right structure includes values like \(E_A = 33.3\), \(E_R = 16.3\). The diagram highlights differences in energy values at specific positions on the rings.
18	Fig9		A 3D plot depicting a spherical space filled with variously sized red and blue spheres, representing data points or particles. The background is a light purple, providing contrast to the spheres. The distribution of spheres appears random, suggesting a simulation or model of particle dispersion within a defined volume.
19	Fig10		Diagram illustrating chemical reactions involving pyrrole in two different processes: xTB nano-reactor and ReaxFF. The xTB nano-reactor process shows pyrrole reacting with hydroxyl radicals, forming intermediates and leading to a

Page no	Fig/Photo	Thumbnail	Alt-text Description
			final product with a hydroxyl group. The ReaxFF process depicts a similar reaction pathway. Initial products include nitrile and carbonyl compounds. Labels include "Pyrrole," "HyATraX," "xTB nano-reactor," "ReaxFF," and "Initial products." Arrows indicate reaction progression.
20	Fig11		Chemical structure diagram showing a polycyclic aromatic hydrocarbon with labeled regions. The structure includes multiple hexagonal rings. Labeled areas include "armchair bay region," "free edge outer quartet," "free edge inner quartet," "fjord region," "outer trio," "inner trio," "zig-zag edge solo," and "K-region duo." Dotted lines and circles highlight specific structural features.
21	Fig12		Chemical structure diagram showing a series of organic compounds with hydroxyl (OH) and carboxyl (COOH) groups. The structures are arranged in two rows, with arrows indicating transformations between them. Numerical values, such as -94.8, -67.1, -113.3, -62.8, -133.0, and -116.6, are associated with each transformation, possibly representing energy changes or reaction conditions. The diagram illustrates chemical reactions and structural changes.
21	Fig13		A reaction energy diagram showing the transformation of chemical structures along a reaction coordinate. The y-axis represents relative energy in kJ/mol, and the x-axis represents the reaction coordinate. The diagram

Page no	Fig/Photo	Thumbnail	Alt-text Description
			includes several chemical structures with energy values: starting at 0.0, then -42.3, -23.5 at the transition state (TS), -66.8, and finally -257.2. The process involves the addition of OH and removal of H2O, CO2, and O2 at different stages. The structures are depicted with hexagonal rings, indicating aromatic compounds.
22	Fig14		Chemical reaction diagram showing a series of transformations involving sulfur-containing compounds. The sequence includes various chemical structures with sulfur atoms, such as thiols, sulfoxides, and sulfones. Arrows indicate the direction of reactions between these compounds. The diagram illustrates the conversion processes and intermediates in sulfur chemistry.
23	Fig15		Chemical structure diagram showing a polycyclic aromatic hydrocarbon composed of five interconnected hexagonal rings. Each ring contains alternating single and double bonds. Numerical values, such as -58.5, -107, and -109, are labeled around the structure, indicating specific properties or measurements related to each hexagon.
24	Fig16		Diagram showing three chemical reaction sequences involving aromatic compounds. \\n\\n1. The first sequence depicts an aromatic compound with hydroxyl and methyl groups reacting with oxygen and hydroperoxyl radicals, resulting in a compound with an aldehyde group.\\n2. The second sequence shows a similar aromatic compound

Page no	Fig/Photo	Thumbnail	Alt-text Description
			reacting with oxygen and hydroperoxyl radicals, forming a compound with a ketone group.\\n3. The third sequence illustrates an aromatic compound undergoing a reaction to form a cyclic compound with a carbonyl group, followed by the release of carbon monoxide.\\n\\nEach sequence highlights structural changes in the chemical compounds.